ELSEVIER

Physics of the Earth and Planetary Interiors 125 (2001) 45–64

PHYSICS OF THE EARTH AND PLANETARY INTERIORS

www.elsevier.com/locate/pepi

Numerical simulations of the cooling of an oceanic lithosphere above a convective mantle

Caroline Dumoulin*, Marie-Pierre Doin, Luce Fleitout

Laboratoire de Géologie, Ecole Normale Supérieure, 24 rue Lhomond, 75231 Paris Cedex 05, France

Received 19 July 2000; received in revised form 16 May 2001; accepted 17 May 2001

Abstract

Numerical simulations of two-dimensional Rayleigh–Bénard convection are designed to study lithospheric cooling above a convective mantle. A strongly temperature- and pressure-dependent viscosity fluid is heated from below or from within. An imposed velocity at the surface of the box mimicks the plate motion between the ridge on one side and the subduction zone on the other side. As the lithosphere cools, its upper part remains rigid and therefore conductive, while its bottom part is convectively unstable. Dripping instabilities are not observed close to the ridge. Nevertheless, the material flows along the slope defined by the lower part of the lithosphere and feeds the first descending drip. Afterwards, cold downgoing instabilities develop continuously and randomly at the base of the lithosphere and are replaced by hot material from the convecting core of the box. The lithosphere continues to thicken even after the onset of the first instability. Surface heat flow, subsidence and lithospheric temperature structure obtained by the convective simulations are compared to the predictions of three conductive models: the Plate, Chablis, and modified Chablis models. These models differ by their applied bottom boundary condition which represents the lithosphere/asthenosphere convective coupling, i.e. by the presence or absence of instabilities developing at the base of the lithosphere. The conductive model which best explains the lithospheric cooling obtained by convective simulations is the modified Chablis model. In this model, a variable heat flow (depending upon the viscosity at the base of the lithosphere) is applied along an isotherm located in the lower unstable part of the lithosphere.

Keywords: Numerical simulation; Oceanic lithosphere; Cooling models

1. Introduction

Oceanic lithospheric cooling can be estimated using bathymetry, surface heat flow and geoid height. The simplest conductive cooling model is the 'half-space' model (Turcotte and Oxburgh, 1967) in which a purely conductive cooling takes place in an infinite rigid half-space. This model fits the bathymetry quite well at young ages (Turcotte and Oxburgh, 1967), but departs at older ages from observations (Davis and Lister, 1974). Indeed, the surface heat flow and the bathymetry at old ages flatten towards asymptotic values (Stein and Stein, 1992). Cazenave and Lago (1991) and Morgan and Smith (1992) assume that this departure may be due to dynamic topography linked to lower mantle mass anomalies or asthenospheric return flows. The flattening has also been explained by the presence of hotspot swells over old seafloors (Crough, 1978), by the effect of phase changes in the cooling lithosphere (Wood and Yuen, 1983), or by heat generation in the lithosphere (Forsyth, 1977). At last, Parsons and McKenzie (1978) consider that the

* Corresponding author. Tel.: +33-1-44-32-22-03; fax: +33-1-44-32-22-00.
E-mail address: dumoulin@geologie.ens.fr (C. Dumoulin).

0031-9201/01/$ – see front matter
PII: S0031-9201(01)00233-3

flattening is due to heat brought to the lithosphere by small-scale convection. The analysis of depth/age and geoid/age relationships at various wavelengths is in favor of heat transfer at the base of the lithosphere to explain the flattening (Doin and Fleitout, 2000). Evidence of small-scale convection may be found in the geoid anomalies in the Center Pacific Ocean and in the South Indian Ocean at young ages (Haxby and Weissel, 1986).

Heat transfer at the base of the lithosphere by small-scale convection has been modelled in simulations of turbulent convection with a strongly temperature-dependent rheology. Due to the high temperature-dependence of the viscosity, the upper part of the thermal boundary layer (t.b.l.), hereafter referred to as the mechanical boundary layer (m.b.l.), is rigid, and instabilities are restricted to a small lower portion of the lithosphere (Buck, 1985). Thermals are believed to detach from the t.b.l. when the Rayleigh number defined locally at the base of the lithosphere grows beyond the critical Rayleigh number (Howard, 1964). The laws governing the heat transfer at thermal equilibrium are now well known for a variety of configurations and rheological laws, i.e. for temperature- and pressure-dependent viscosities, Newtonian and non-Newtonian rheologies, and different heating modes (Davaille and Jaupart, 1993; Solomatov, 1995; Doin et al., 1997; Dumoulin et al., 1999; Grasset and Parmentier, 1998; Solomatov and Moresi, 2000). These numerical or analogical experiments show that the viscosity at the base of the lithosphere must be of the order of 10^{18}–10^{19} Pa s in order to lead to an equilibrium thickness of the lithosphere of about 100 km (Dumoulin et al., 1999; Fleitout and Yuen, 1984).

Numerical simulations or analogical experiments have been performed to study the onset of small-scale convection. With an exponentially depth-dependent rheology inducing a permanent stiff layer at the top of the box, convective instabilities develop at the base of the lithosphere after 70 Ma for an asthenospheric viscosity close to that found with the post-glacial rebound (about 10^{20} Pa s) (Jaupart and Parsons, 1985). However, such a viscosity at the base of the lithosphere leads to values which are too large for the equilibrium thickness of the lithosphere. A lower viscosity beneath the ridge enables positive growth rates of the instabilities at younger ages (Yuen and Fleitout, 1984; Buck and Parmentier, 1986). It remains compatible with the upper mantle viscosity derived from post-glacial rebound studies as the viscosity depends strongly on temperature and pressure. After an early destabilization of the lithospheric base, the lithosphere may continue to thicken by conductive cooling (Fleitout and Yuen, 1984). However, in the analogical experiments of Davaille and Jaupart (1994), instabilities develop at the base of the lithosphere only after 40–65 Ma even in the case of low asthenospheric viscosity. As results differ from one study to another, it appears that the onset of instabilities at the base of a cooling lithosphere is still not a well-constrained process and that its mechanism is still not fully understood.

Topography, heat flow, and geoid variations with time are well described by two conductive models with heat input at the base of the lithosphere, the Plate model (Parsons and McKenzie, 1978) and the Chablis model (Doin and Fleitout, 1996), which will both be defined in detail in Section 3. It is assumed that, in the first model, the onset of small-scale convection occurs at about 70 Ma, whereas in the second model, small-scale convection develops at all ages.

The aim of this study is to discriminate by 2-D numerical simulations which conductive model best explains the lithospheric cooling obtained on top of a convective mantle. We will first present the convective simulations, and describe the development of instabilities at the base of the t.b.l. We will then introduce conductive models, and at last, compare the variations with the age of the lithosphere of surface heat flow, subsidence, and temperature structure between convective simulations and conductive models.

2. Description and results of the convective simulations

2.1. Setup of the numerical experiments

We consider two-dimensional convection in a Boussinesq fluid with an infinite Prandtl number. The code built by Christensen (1983) and Christensen (1984) solves the equations of conservation of mass, energy, and momentum. We neglect viscous dissipation and adiabatic heating. All variables are normalized using the height of the convective box D and a temperature drop ΔT (see Tables 1 and 2), and are

Table 1
List of symbols

Constant	Symbol
Box height	D
Temperature drop across the box	ΔT
Thermal conductivity	k
Thermal diffusivity	κ
Thermal expansion coefficient	α
Mantle density	ρ
Water density	ρ_w

denoted with exponent *. The fluid is either heated from within or from below. The temperature is fixed at the top boundary ($T_t^* = 0$). In bottom heated cases, the temperature is also fixed at the bottom ($T_b^* = 1$), whereas in internal heated cases, the radiogenic heat production (H^*) is fixed and the box base is insulated. When the fluid is heated from within, the temperature inside the core flow (T_i^*) varies until the surface heat flow is statistically equal to the radiogenic heat production in the box ($q^* = H^*$). In all cases, the sides are insulated. To simulate lithospheric cooling from a ridge at the right side of the box (zone of divergence) to a subduction zone (i.e. zone of convergence), a velocity is imposed on the first two top grid elements. The right plate defined by $x^* > 0.5$ is moving with a uniform velocity V^* towards the left, whereas the left plate with $0 < x^* < 0.5$ moves towards the right. This results in a zone of convergence at $x^* = 0.5$ and two zones of divergence on both sides of the box. Boundary conditions on the bottom and sides of the box are free slip.

To ensure that the upper part of the lithosphere will remain rigid and therefore conductive, we choose high viscosity contrasts, with a viscosity depending exponentially on temperature and pressure

$$\nu^*(T^*, z^*) = \frac{\nu}{\nu_0} = \exp(-bT^* + cz^*) \quad (1)$$

where ν_0 is the surface viscosity, $b = 13.0$ (corresponding to a total viscosity contrast of 4×10^5), and $c = 0$ or 4.2 (corresponding to a total viscosity contrast ranging from 1 to 66.7). In rigid lid convection, it has been shown that the effective temperature drop through the dynamically active part of the lithosphere derives from the viscous temperature scale

Table 2
Variable normalizations[a]

Variable	Corresponding symbols	Box normalization	Lithosphere normalization
Depth	z	$z^* = \frac{z}{D}$	$z^{**} = \frac{z}{z_{eq}}$
Age	t	$t^* = \frac{\kappa t}{D^2}$	$t^{**} = \frac{\kappa t}{z_{eq}^2}$
Temperature	T	$T^* = \frac{T}{\Delta T}$	$T^{**} = \frac{T}{T_i}$
Heat flow	q	$q^* = \frac{qD}{k\,\Delta T}$	$q^{**} = \frac{qz_{eq}}{kT_i}$
Internal temperature	T_i	$T_i^* = \frac{T_i}{\Delta T}$	$T_i^{**} = 1$
Effective temperature drop	δT_{eff}	$\delta T_{eff}^* = \frac{\delta T_{eff}}{\Delta T}$	$\delta T_{eff}^{**} = \frac{\delta T_{eff}}{T_i}$
Cut-off temperature	$T_q = T_i - \delta T_{eff}$	$T_q^* = T_i^* - \delta T_{eff}^*$	$T_q^{**} = 1 - \delta T_{eff}^{**}$
Thermal equilibrium thickness	z_{eq}	$z_{eq}^* = \frac{z_{eq}}{D}$	$z_{eq}^{**} = 1$
Surface velocity	V	$V^* = V\frac{D}{\kappa}$	$V^{**} = V\frac{z_{eq}}{\kappa}$
Radiogenic heat production	H	$H^* = \frac{HD^2}{k\,\Delta T}$	$H^{**} = \frac{Hz_{eq}^2}{kT_i}$
Subsidence	ω	$\omega^* = \frac{(\rho - \rho_w)\omega}{\rho\alpha\,\Delta T\,D}$	$\omega^{**} = \frac{(\rho - \rho_w)\omega}{\rho\alpha T_i z_{eq}}$

[a] Single asterisk (*): variable normalized on the convecting box; double asterisk (**): variable normalized on the lithosphere at equilibrium.

Table 3
Presentation of the variables characterising each simulation

Simulation number	c	Ra_0	H^*	V^*	V (cm a^{-1})	U^*	T_i^*	t_{inst}^* (Ma)	t_{inst}	Ra_{BL}
1	0	3000	5.5	75	0.28	247	0.660	0.0039	68.7	1.60×10^7
2	0	4000	6.5	100	0.33	341	0.675	0.0028	65.7	2.57×10^7
3	0	5500	7.5	280	0.92	251	0.615	0.0030	70.4	1.63×10^7
4	4.2	1550	5.6	50	0.23	213	0.750	0.0048	58.7	1.68×10^7
5	4.2	2480	6.25	50	0.20	312	0.759	0.0042	65.0	3.14×10^7
6	4.2	5000	7.5	150	0.49	300	0.700	0.0016	37.5	3.07×10^7
7	4.2	5000[a]	7.5	150	0.45	429	0.734	0.0014	38.5	4.71×10^7
8	4.2	5000[a]	7.5	300	0.98	320	0.699	0.0016	37.5	2.86×10^7
9	4.2	5000[b]	7.5	600	1.97	384	0.653	0.0035	82.1	1.84×10^7
10	4.2	9900	11.25	380	0.96	403	0.723	0.0009	35.7	8.37×10^7
11	4.2	1550	0	50	0.23	460	0.791	0.0019	23.2	3.33×10^7
12	4.2	2480	0	150	0.83	469	0.732	0.0015	12.3	2.56×10^7
13	4.2	5000	0	150	0.45	739	0.756	0.0007	19.3	7.09×10^7
14	4.2	9900	0	280	0.64	902	0.736	0.0005	24.5	1.14×10^8
15	4.2	9900	0	380	1.05	934	0.726	0.0007	22.9	9.50×10^7
16	4.2	9900	0	500	1.51	882	0.720	0.0008	22.0	9.09×10^7

[a] Simulation with a 501×51 grid and for an aspect ratio of 8.
[b] Simulation with a 676×51 grid and for an aspect ratio of 10.

$T_\nu^* = (-\partial \ln \nu^*/\partial T^*)^{-1}$ (Morris and Canright, 1984; Nataf, 1986). This temperature drop has been measured experimentally by Davaille and Jaupart (1993) and numerically by Grasset and Parmentier (1998), and found equal to $2.24T_\nu^* = 2.24b^{-1}$. Each simulation is characterized in Table 3 by the value of the viscosity pressure dependence c, the Rayleigh number Ra_0 defined as $(\alpha\rho g\Delta T D^3)/(\kappa\nu_0)$, the velocity V^* imposed at the surface, and the value of H^* for internally heated simulations. Ra_0 can be related to the only free parameter for convection in an internally heated fluid, $Ra_{H-0} = (\alpha\rho g H D^5)/(\kappa k \nu_0)$ using $Ra_{H-0} = Ra_0 H^*$.

The box is divided into 251×51 cells for aspect ratios of 4, into 501×51 cells for aspect ratios of 8, and into 676×51 cells for aspect ratio of 10. In

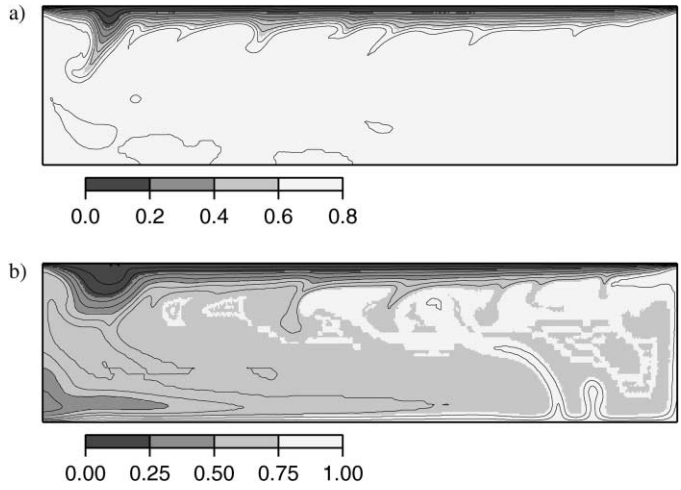

Fig. 1. Examples of temperature T^* fields for (a) an internal heated simulation with $Ra_0 = 2480$, $V^* = 50$, and $c = 4.2$, and (b) a bottom heated simulation with $Ra_0 = 2480$, $V^* = 150$, and $c = 4.2$. Isotherms are drawn every temperature step of 0.1 (black lines).

the high aspect ratio grids, the horizontal spacing is smaller near the ridge, otherwise it is uniform. In order to increase the accuracy in the lithosphere, the grid is denser in the upper third of the box.

The variables averaged on the entire box (for example, T_i^*, q^*) having reached a statistical steady state, we analyse the results of the convective simulations using 'movies' showing the temperature and stream function fields.

2.2. Description of the flow

As the lithosphere cools from the ridge to the subduction zone, numerous small-scale instabilities develop from the unstable rheological sublayer at its base (cf. Figs. 1 and 2). These instabilities slow down the cooling of the lithosphere, as cold material dripping from the base of the lithosphere are replaced by hot asthenospheric material. This phenomenon transfers heat upwards. For appropriate aspect ratio, surface velocity V^*, and Rayleigh number Ra_0, the lithosphere reaches an equilibrium thickness, z_{eq}^*, before it subducts. This equilibrium is obtained when the heat transfered by small-scale instabilities equals the heat conducted through the rigid lid. Cold blobs may detach from the lithosphere, when their size is sufficiently large and if the interior velocity is low enough. In other cases, small-scale downwellings form continuous long drips stretched downwards. In all cases this cold material is advected into the mantle and disappears by stretching and heat diffusion.

Both the dripping of small-scale instabilities and the imposed plate subduction act to cool the interior. However, in the simulations presented here, a statistically steady state is reached where this cooling is on average compensated by internal heating or bottom heating. In simulations where the cooling by subduction of the lithosphere dominates, the interior temperature T_i^* decreases with V^*, whereas in simulations mainly cooled by small-scale instabilities, we obtain a higher value for T_i^* (this value depends on T_v^* and c). Therefore, the interior temperature T_i^* will depend, in our simulations, on the ratio between the heat transfers by the two heat transfer mechanisms. For a given aspect ratio and a given Ra_0, a higher surface velocity will then yield a smaller interior temperature (compare simulations 7 and 8). On the other hand, for a given surface velocity and a given Ra_0, a larger aspect ratio will yield a higher interior temperature. Indeed, the heat transfered by subduction remains constant but the heat transfered by instabilities increases with the box width (compare simulations 6 and 7).

Time series of simulations snapshots show that these small-scale instabilities interact with the topography

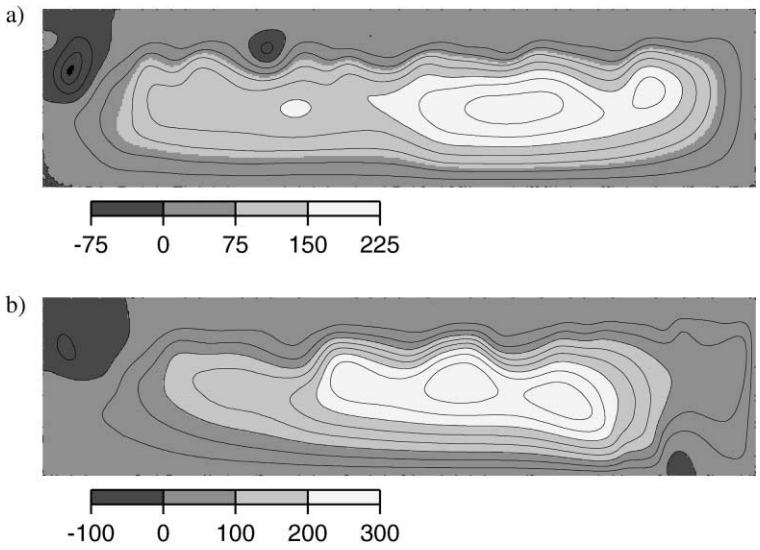

Fig. 2. Examples of stream function fields for (a) an internal heated simulation with $Ra_0 = 2480$, $V^* = 50$, and $c = 4.2$, and (b) a bottom heated simulation with $Ra_0 = 2480$, $V^* = 150$, and $c = 4.2$.

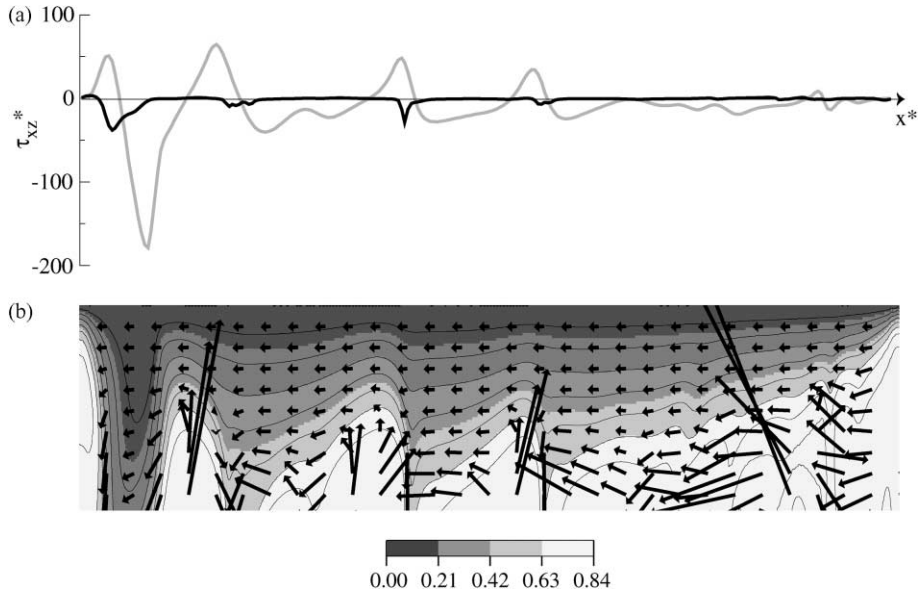

Fig. 3. (a) Two horizontal shear stress (τ_{xz}^*) profiles for simulation 13, estimated at the top of the box, τ_t^* (gray curve) and estimated at the thickness of thermal equilibrium, τ_b^* (black curve). (b) Zoom on the lithosphere temperature T^* structure for simulation 13. Black arrows represent the velocity field. The height of the displayed lithospheric cross-section is 0.14 (vertical exaggeration is of 7).

of the isotherms within the conductive part of the lithosphere. When a drip first develops, it deflects downwards, by advection in the rheological sublayer and by conduction in the rigid lid, the isotherms located above it. The whole system (drips and downwards deflected isotherms) drifts then together with the plate motion. The localized flow in the rheological sublayer follows the slope defined by isotherms topography and results in dripping instabilities at topographical tips (see Fig. 3). As lithospheric age increases, isotherms topography becomes more pronounced and affects the whole conductive lithosphere.

2.3. Shearing by large scale circulation

A large-scale circulation, with an asthenospheric flow going from beneath the ridge towards the subducting plane, is superimposed over the small-scale flow (see Fig. 2). Its velocity U^*, averaged in areas with temperature $>0.7T_i^*$, is deduced from the stream function averaged through time. In simulations described in Table 3, it is in general larger than the imposed surface velocity V^*. Such a large-scale flow, driven by the presence of a cold slab on the left side of the box, has also been observed experimentally in a tank with a cold sidewall by Nataf et al. (1981). It induces a shearing of the lithospheric base and yields an asymetrical shape for the instabilities and lithospheric isotherms topography (see Figs. 1 and 3). In bottom heated simulations, hot plumes of variable size and position develop from the bottom thermal boundary layer, and feed the asthenosphere with hot material. Because the sinking slab covers a large part of the bottom thermal boundary layer, because of the free slip boundary condition applied on the box sides, and because of the divergence imposed at the surface, the main plume upwelling occurs on the right side of the box, beneath the ridge. The plume buoyancy increases the strength of the large-scale circulation.

Let us call "free convective velocity", the velocity of the large scale flow that we would obtain using the same temperature field as in our simulations (for example, Fig. 1) but a no slip boundary condition at the top of the box. This velocity should depend on the Rayleigh number, i.e. on the core flow viscosity and on the temperature contrasts between slab, plume, and core. If the imposed plate velocity V^* is larger than the free convective velocity, it will force the flow inside the box, as shown by Lux et al. (1979) in a similar setting and at low Rayleigh numbers. In this case, we expect

an interior velocity U^* scaling with V^*. Sublithospheric flow is then driven by plate movement and induces a resistive shearing at the base of the lithosphere. This occurs only in simulation 9. If we set a surface velocity V^* lower than the free convective velocity, the interior velocity U^* will depend mostly on the Rayleigh number. This is the case in most of our simulations except 3 and 8–10. The flow in the asthenosphere is then faster than the plate velocity. The ratio U^*/V^* varies in our simulations between 0.6 and 12.

We computed in three cases (simulations 9, 13, and 16), the shear stress at the thickness of the thermal lithospheric equilibrium (z^*_{eq}) τ^*_b and at the top of the box τ^*_t (see Fig. 3). The negative stress calculated on top implies that the top boundary condition counteracts lithospheric motion. Due to the strong viscosity contrast between the bottom and the top of the lithosphere, τ^*_b is very small compared to τ^*_t. A simple force balance indicates that the basal shear stress is too low to really promote lithospheric motion. Therefore, the main driving forces are, in our simulations, the ridge push and slab pull forces. Low shear stress at the base of the oceanic lithosphere is compatible with observations of stress orientations on Earth (Bird, 1998).

As we impose the surface velocity V^*, we may wonder which values should be chosen to obtain realistic flows. Asthenospheric flow should depend on the upper mantle viscosity and buoyancy sources in the upper mantle, whereas plate motion should mainly depend on the strength of convergence zone and on ridge push and slab pull forces (King and Hager, 1990; Zhong et al., 1998). Modeling a plate-like behavior in convection simulations requires rheologies that are not only strongly temperature-dependent but that also strongly localize strain along self developping "weak zones" (see review in Tackley, 2000). Here, the chosen rheology is a reasonable approximation of mantle rheology at high temperature, and thus enables a good description of processes taking place at the base of the lithosphere or within the mantle. Kameyama and Ogawa (2000), using a rheology similar to ours and a free surface boundary condition, obtain a sublithospheric shearing oriented towards the subduction zone. However, at low temperature, this rheology is not realistic and do not yield realistic lithospheric deformation and convergence pattern. One way to obtain a plate-like behavior and a free surface motion would have been to add a weak zone. However, the resulting U^*/V^* ratio remains arbitrary as it should strongly depend on the chosen "friction coefficient" along the fault. As the strength of the subduction plane with respect to the surrounding material is still unknown, we cannot infer what should be the direction and intensity of shearing on Earth. As we will see below, the cooling of the lithosphere is not influenced by the U^*/V^* ratio.

2.4. The first dripping instabilities

No dripping instabilities are seen very close to the ridge. We determine the age of the first dripping instability, t^*_{inst}, by simple observations of temperature field pictures. Therefore, it may be overestimated (Table 3). The t^*_{inst} decreases with Ra_{BL}, the Rayleigh number calculated with the viscosity ν_{BL} at the depth z^*_{BL} where the youngest instability develops ($Ra_{BL} = Ra_0 \exp(bT^*_i - cz^*_{BL})$), but the relationship is fuzzy and we did not find any well defined exponent in $t^*_{inst} \propto Ra_{BL}$.

In rigid lid convection, the surface heat flow is proportionnal to $Ra^{1/3}_{BL}$. Therefore, the equilibrium lithospheric thickness, z_{eq}, does not depend on the dimentionalized height of the box D and of the flow structure (convection in one or two layers). Consequently, we can scale the height of the box D assuming that the equilibrium thickness of the oceanic lithosphere z_{eq} is 100 km, thus yielding $D = z_{eq}/z^*_{eq}$. The z^*_{eq} for each simulation is presented in Table 5. The age of the first dripping instability t_{inst} and the imposed surface velocity V are then dimentionalized using D and a thermal diffusivity of $8 \times 10^{-7}\,m^2\,s^{-1}$. The age t_{inst}, in our simulations, varies between 10 and 80 Ma. Having no relationship between t_{inst} and the other parameters of the convection, we do not propose an age of first dripping instability for the Earth. No clear correlations between t^*_{inst} and velocities V^* or U^* are observed. However, we note that the lithosphere continues to cool, and therefore to thicken, after the first instability (compare Figs. 1 and 5a).

Fast cooling near the ridge is responsible for the steep shape of the lithosphere. As mentioned above, we do not observe instabilities close to the ridge. However, between the ridge and the first instability, velocities inside the lower part of the lithosphere follow the geometry of the isotherms (see Fig. 4). The material at the base of the lithosphere flows faster than the rigid upper part and, following the lithosphere

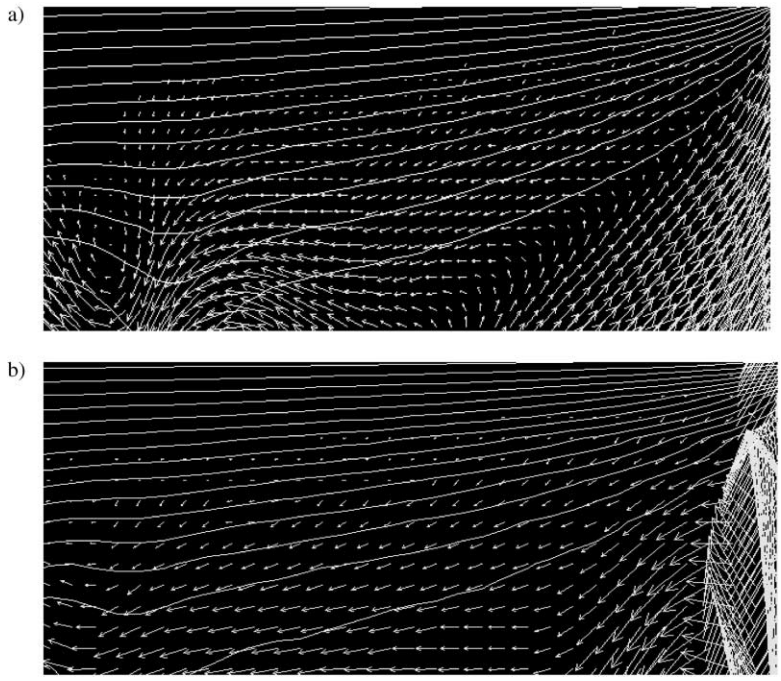

Fig. 4. Zoom on the lithosphere temperature T^* structure through a young lithosphere for (a) an internal heated simulation with $Ra_0 = 5000$, $V^* = 300$, and $c = 4.2$, and (b) a bottom heated simulation with $Ra_0 = 9900$, $V^* = 500$, and $c = 4.2$. Isotherms are drawn every temperature T^* step of 0.05. White arrows represent the velocity vectors in the moving reference of the plate. Vertical exaggeration is of 3. The width and height of the displayed lithospheric cross-section are 0.6 and 0.09, respectively.

shape, feeds the first instability. Therefore, even if no instabilities are seen at very young ages, the lower part of the lithosphere is unstable. Note that this phenomenon cannot be observed in transient cooling studies. The amplitude of the velocity inside the base of the lithosphere could be due to finite density perturbations created by the presence of the slope or to viscous coupling. In some simulations, we can clearly see that the material is flowing inside the base of the lithosphere away from the ridge whereas the material underneath is rising in the opposite direction (see Fig. 4a). Moreover, the viscosity at the base of the lithosphere is small and, in consequence, does not favor a strong viscous coupling. This basal flow is therefore not produced by viscous coupling.

2.5. Average lithospheric cooling

In order to compare the lithospheric cooling in convective simulations and in conductive cooling models, we average the temperature field with time (see an example for simulation 12 in Fig. 5). This process smoothes out the variability due to the development of small-scale instabilities at the base of the lithosphere. The subsidence ω^* and surface heat flow q^* are calculated from this average temperature field. We define a cut-off temperature T_q^* which enters in the subsidence calculation, $\omega^* = \int_0^{T_q^*} (T^* - T_i^*)\,\mathrm{d}z^*$. We choose $T_q^* = T_i^* - \delta T_{eff}^*$, where $\delta T_{eff}^* < 2.24b^{-1}$, to take into account the fact that the lower part of the t.b.l. is both conductive and convective (see Section 3 for more details). For all simulations, q^* and ω^* decrease from the ridge to the subduction zone and, in many simulations, flatten before reaching the convergent plate boundary. The variations with age of subsidence, surface heat flow, and temperature inside the lithosphere will then be compared to the cooling models predictions. To evaluate the influence of the grid spacing on T^*, q^*, and ω^*, a convergence test is performed in a case where the fluid is heated from below (see Table 4). Root mean square (RMS) dif-

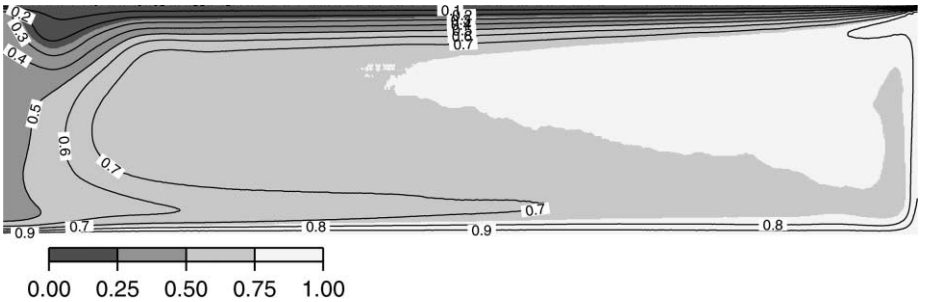

Fig. 5. Example of time-averaged temperature T^* field for a bottom heated simulation ($Ra_0 = 2480$, $V^* = 150$, and $c = 4.2$). Isotherms are drawn every temperature T^* step of 0.1 (black lines).

Table 4
Convergence test done for $Ra_0 = 9900$, $c = 4.2$, and $V^* = 380$ in the bottom heating mode

Grid	T_i^*	Comparison on $1/q^*$, RMS	Comparison on ω^*, RMS
251×51[a]	0.728	0.00242	0.00132
251×51[b]	0.724	0.00409	0.00417
501×101[b]	0.725	–	–

[a] Vertical grid denser in the lithosphere, uniform horizontal grid spacing.
[b] Vertical grid denser in the lithosphere, horizontal grid denser near the ridge.

ferences between $1/q^*$ and ω^* for the reference case (501×101 grid) and $1/q^*$ and ω^* resulting from two other computations with larger grid spacing are calculated. These RMS differences give an uncertainty estimate useful to measure the quality of the fits between convective results and conductive models predictions, which are presented in Section 4.

3. Description of the cooling models

In this study, the predictions of the Plate, Chablis, and modified Chablis conductive models will be compared with the results of convective simulations. All cooling models are solutions to the two-dimensional equation of heat conduction in a vertical plane of symmetry

$$\frac{\partial T^{**}}{\partial t^{**}} = \frac{\partial^2 T^{**}}{\partial (z^{**})^2} + \frac{1}{(V^{**})^2}\frac{\partial^2 T^{**}}{\partial (t^{**})^2} + H^{**} \qquad (2)$$

where all variables are normalized on the lithosphere using the thickness of the lithosphere at equilibrium z_{eq} and the temperature inside the core flow T_i (see Table 2); V^{**} is the surface velocity, T^{**} the temperature, z^{**} the depth, t^{**} the lithosphere age, and H^{**} is the volumetric heat production. The initial condition for all three conductive models is an isothermal mantle ($T^{**} = 1$). We thus consider that the mantle below the ridge has a constant temperature equal to the internal temperature T_i^*. The differences between the models result from the bottom boundary condition.

In the Plate model, the conductive, rigid part of the upper mantle is assumed to have a constant thickness. A constant temperature $T^{**} = 1$ (maintained by convection in the mantle) is applied at its bottom. The temperature field of the lithosphere for the Plate model is drawn in Fig. 6. The bottom boundary condition of the Plate model implies a heat transfer from the asthenosphere to the rigid plate increasing with time.

In the Chablis model, the bottom boundary condition is a constant heat flow applied inside the lower part of the lithosphere, in order to mimic small-scale convection whatever the age (Doin and Fleitout, 1996). In this model, the t.b.l. structure is simplified, as shown by the comparison between Fig. 7a and b. It is divided into a purely rigid and conductive upper part (above the isotherm T_q^{**}) and an unstable bottom part ($T_q^{**} < T^{**} < 1$). A constant heat flow ($q_{m0}^{**} = 1$ for bottom heated cases and $q_{m0}^{**} < 1$ for internally heated cases) is applied at a constant temperature $T_q^{**} = 1 - \delta T_{eff}^{**}$, where δT_{eff}^{**} is the temperature drop across the unstable layer. Note that the depth of the isotherm T_q^{**} increases with age. An effective temperature drop, normalized by T_i, of about $2.24(bT_i^*)^{-1}$ (where $\exp(bT_i^*)$ is the viscosity contrast across the lithosphere) characterizes the unstable layer at the base of the t.b.l. We

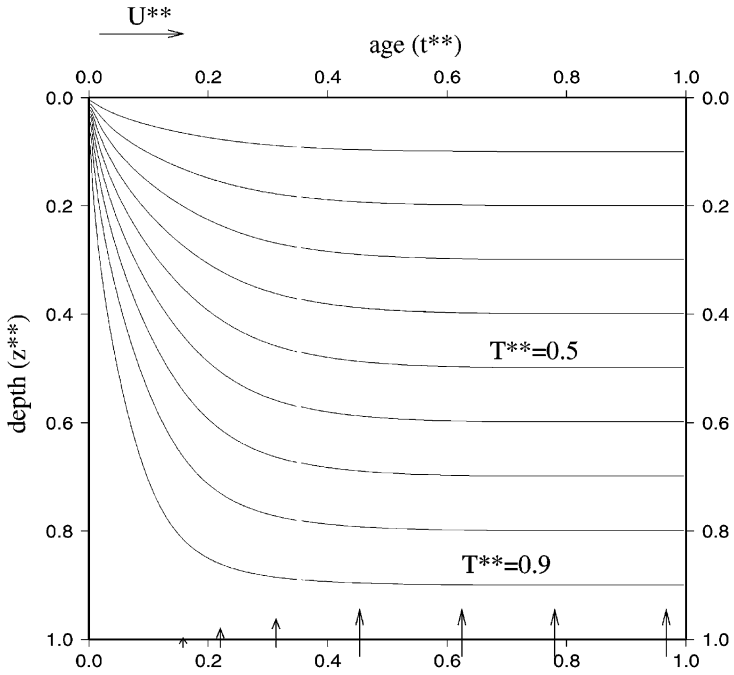

Fig. 6. Temperature (T^{**}) structure obtained with the Plate model for a heated from below case. Isotherms (black lines) are displayed as a function of age. Black arrows symbolize the increasing heat transfer brought by small-scale convection at depth $z^{**} = 1$.

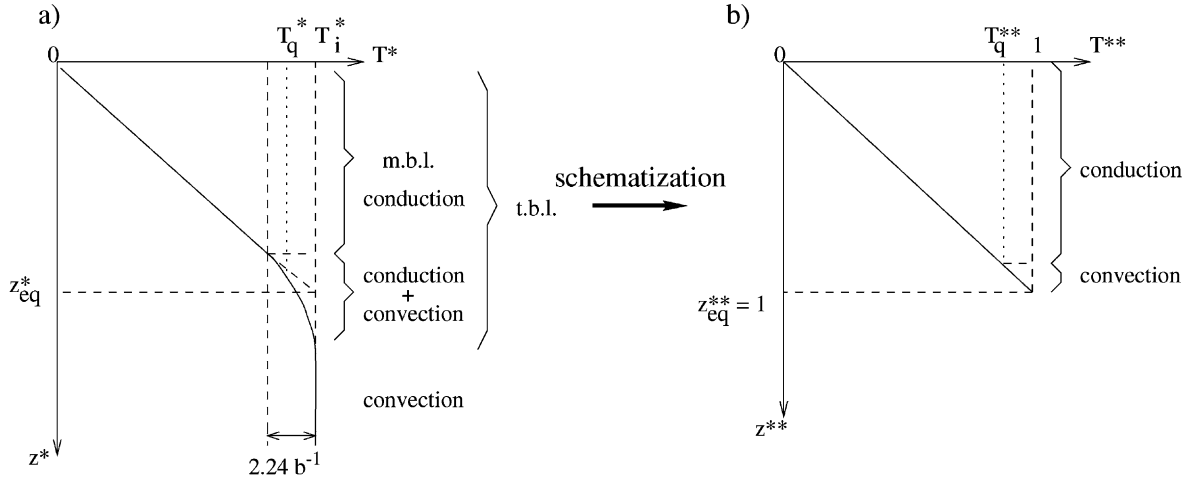

Fig. 7. Sketch of temperature profiles at equilibrium for heated from below cases (a) for convective simulations ($T^*(z^*)$) and (b) for the Chablis and modified Chablis models ($T^{**}(z^{**})$). The t.b.l. in convective simulations present a rigid purely conductive m.b.l. plus a partly conductive and partly convective unstable bottom layer. This t.b.l. is simplified in the Chablis and modified Chablis models by a thicker purely conductive layer and a thin purely convective bottom layer.

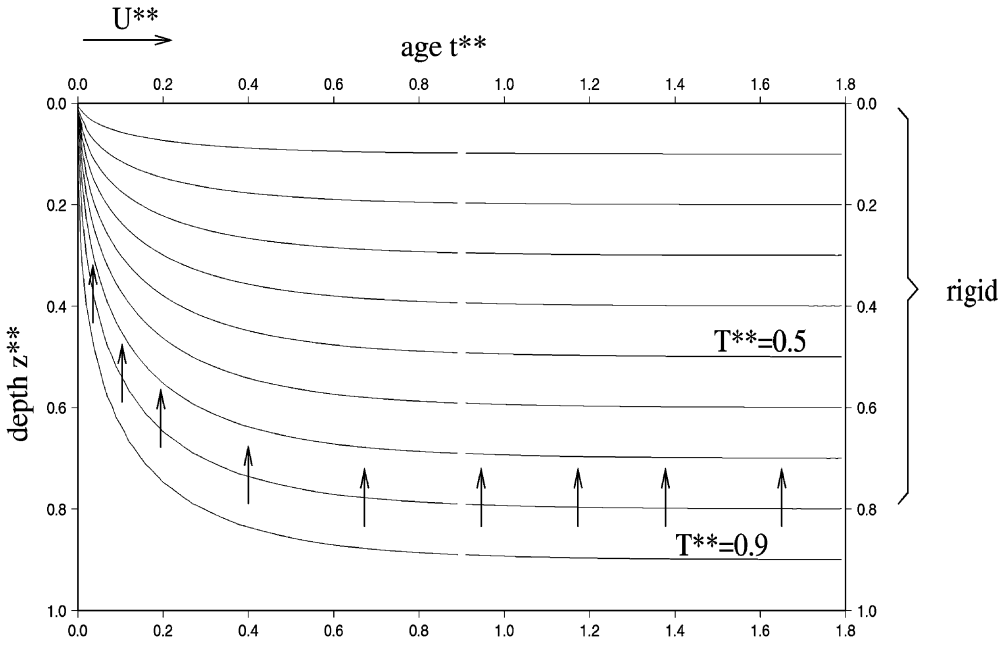

Fig. 8. Temperature (T^{**}) structure obtained with the Chablis model for a heated from below case. Black lines are isotherms. Black arrows symbolize the constant heat transfer brought by small-scale convection at the base of the mechanical boundary layer.

choose a smaller temperature drop to represent the strictly convective part of the thermal boundary layer: $\delta T_{\mathrm{eff}}^{**} = 1.65(bT_{\mathrm{i}}^{*})^{-1}$. Indeed, the coefficient of 1.65 yields better fits between Chablis and modified Chablis model predictions and simulations results than coefficients of 2.24 or 1.12. A steady state conductive geotherm is used to compute the temperature between the depth of the isotherm $T^{**} = T_{\mathrm{q}}^{**}$ and the depth of the isotherm $T^{**} = 1$. The temperature field of the lithosphere for the Chablis model is depicted in Fig. 8.

Convection simulations with temperature- and pressure-dependent viscosity show that the heat flow across the lithosphere in thermal equilibrium due to the destabilization of its base is directly proportional to the asthenospheric viscosity to the power 1/3 (Doin et al., 1997; Dumoulin et al., 1999). However, in our simulations, this bottom heat flow may vary laterally with the viscosity at the base of the lithosphere because of the pressure dependence of the rheology and the asthenospheric temperature changes. Therefore, the Chablis model has been modified to include a heat flow applied along the isotherm $T^{**} = T_{\mathrm{q}}^{**}$ and q_{m}^{**}, that is no longer constant but decreases with the depth of this isotherm z_{is}^{**}. The function $q_{\mathrm{m}}^{**}(z_{\mathrm{is}}^{**})$ is constructed by analysing the lateral viscosity contrast due to temperature (as in Eberle and Forsyth, 1995) and depth changes at the base of the cooling lithosphere in convection simulations.

For a fluid heated from within, the temperature at the base of the lithosphere decreases regularly with age t^{*} from the ridge to the convergent plate boundary (see, for example, in Fig. 9). The heat transfer at $T^{**} = T_{\mathrm{q}}^{**}$ is then written as follow:

$$
\begin{aligned}
q_{\mathrm{m}}^{**}(z_{\mathrm{is}}^{**}) &= q_{\mathrm{m0}}^{**}\left(\frac{\nu(z_{\mathrm{is}}^{**})}{\nu(z_{\mathrm{q}}^{**})}\right)^{1/3} \\
&= q_{\mathrm{m0}}^{**}\exp\left(\frac{cz_{\mathrm{eq}}^{*}}{3}\left(1-\frac{z_{\mathrm{is}}^{**}}{z_{\mathrm{q}}^{**}}\right)\right. \\
&\quad \left.+\frac{b\delta T_{0}^{*}}{3}\left(1-\left(\frac{z_{\mathrm{is}}^{**}}{z_{\mathrm{q}}^{**}}\right)^{2}\right)\right) \qquad (3)
\end{aligned}
$$

where δT_{0}^{*} is an estimate of the lateral temperature variation under the lithosphere (see Fig. 9) and z_{q}^{**} is the depth of the isotherm T_{q}^{**} at equilibrium. When the viscosity does not depend on pressure ($c = 0$), the

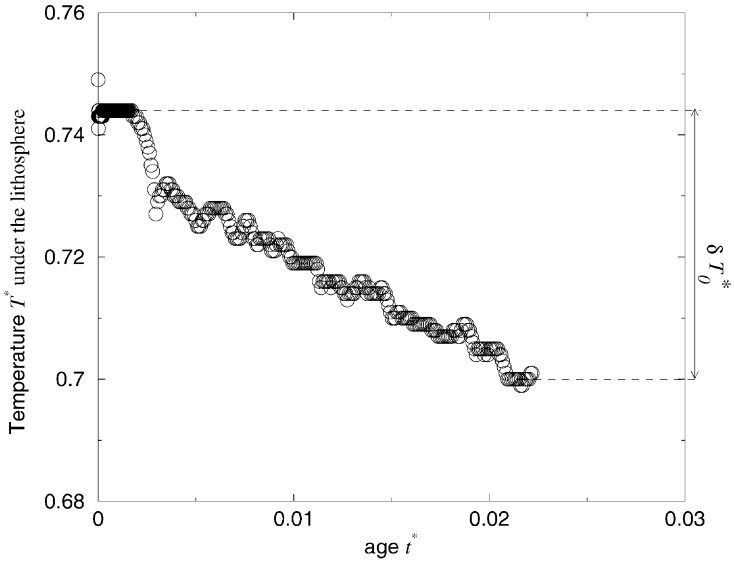

Fig. 9. Variations of the asthenospheric temperature (T^*) as a function of age (t^*) for an internally heated fluid ($Ra_0 = 5000$, $U^* = 300$, and $c = 4.2$).

Chablis and modified Chablis models are very close. Indeed, $q_m^{**}(z_{is}^{**})$ then takes into account only temperature variations in the asthenosphere, which in these cases are small.

In the bottom heated cases, an important plume at the ridge induces large viscosity variations at the base of the lithosphere near the ridge (see Fig. 10). The viscosity increases more quickly between $z_{is}^{**} = 0$ and

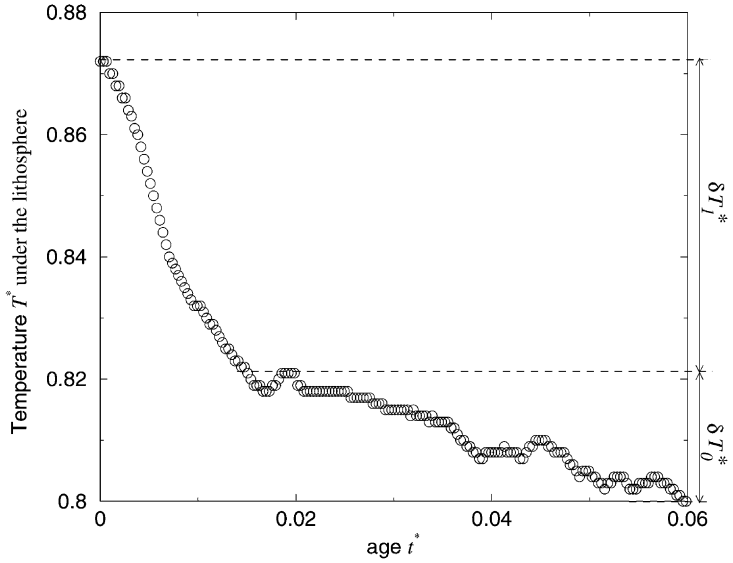

Fig. 10. Variations of the asthenospheric temperature (T^*) as a function of age (t^*) for a bottom heated fluid ($Ra_0 = 1550$, $U^* = 50$, and $c = 4.2$); ($\delta T_0^* + \delta T_1^*$) is an estimate of the lateral temperature veriation under the lithosphere and δT_1^* corresponds to the increase in asthenospheric temperature due to the plume ascending below the ridge.

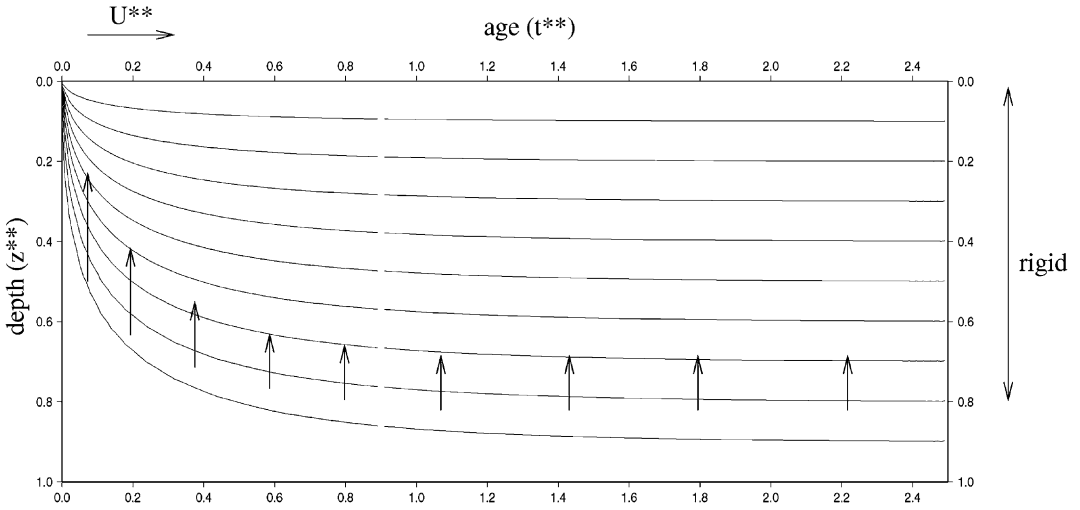

Fig. 11. Temperature (T^{**}) structure obtained with the modified Chablis model for a bottom heated case. Black lines are isotherms. Black arrows symbolize the heat transfer brought by small-scale convection at the base of the mechanical boundary layer and decreasing with depth.

$3z_q^{**}/4$ (arbitrary value) than between $z_{is}^{**} = 3z_q^{**}/4$ and z_q^{**}. Therefore, the heat transfer applied inside the lower part of the lithosphere writes as follow:

$$q_m^{**}(z_{is}^{**}) = q_{m0}^{**} \exp\left(\frac{cz_{eq}^{*}}{3}\left(1 - \frac{z_{is}^{**}}{z_q^{**}}\right) + \frac{b\delta T_0^{*}}{3}\left(1 - \left(\frac{z_{is}^{**}}{z_q^{**}}\right)^2\right)\right), \quad \text{for } z_{is}^{**} > \frac{3z_q^{**}}{4} \tag{4}$$

and

$$q_m^{**}(z_{is}^{**}) = q_{m0}^{**} \exp\left(\frac{cz_{eq}^{*}}{3}\left(1 - \frac{z_{is}^{**}}{z_q^{**}}\right) + \frac{b\delta T_0^{*}}{3}\left(1 - \left(\frac{z_{is}^{**}}{z_q^{**}}\right)^2\right) + \frac{b\delta T_1^{*}}{3}\left(1 - \left(\frac{4z_{is}^{**}}{3z_q^{**}}\right)^2\right)\right), \quad \text{for } z_{is}^{**} < \frac{3z_q^{**}}{4} \tag{5}$$

where δT_0^{*} and δT_1^{*} are defined in Fig. 10. An example of lithospheric temperature field obtained for the modified Chablis model is represented in Fig. 11.

For the three models, the equation of heat conduction is solved by the finite differences technique and the Gauss–Seidel method. Grids being divided into 251×26 cells, they allow a better accuracy than grids of the convective simulations. Indeed, in the latter, only 10–15 points of grid are located inside the lithosphere. Note that in the three conductive models, the thermal equilibrium state is the same ($T^{**} = z^{**}$ for bottom heated cases and $T^{**} = -(H^{**}/2)(z^{**})^2 + ((H^{**}/2)+1)z^{**}$ for internally heated cases). The difference between the three conductive models is the characteristic cooling time. The lithosphere reaches thermal equilibrium about two times faster in the Plate model than in the Chablis model, and in the Chablis model than in the modified Chablis model (compare Figs. 6, 8 and 11).

4. Comparison of the different models

We compare the surface heat flow, subsidence, and temperature structure from the three conductive models to those obtained by the convective simulations. Temperature structures are computed, for all conductive models, with surface velocity set to $V^{**} = V^{*}z_{eq}^{*}$, with a volumetric heating set to $H^{**} = H^{*}(z_{eq}^{*})^2/T_i^{*}$, and for the modified Chablis model, with values of δT_0^{*} and δT_1^{*} (presented in Table 5) that pertain to

Table 5
Data for the fits between simulations and the modified Chablis model and estimates of the equilibrium heat transfer

Simulation number	δT_0^*	δT_1^*	q_{eq}^*	$q_{eq-conv}^*$	$q_{eq-calc}^*$	z_{eq}^*
1	0.020	–	4.70	4.70	5.02	0.15
2	0.017	–	5.50	5.54	5.79	0.13
3	0.026	–	5.20	<5.19	5.23	0.13
4	0.045	–	4.70	4.74	5.33	0.18
5	0.037	–	5.35	5.41	6.33	0.16
6	0.027	–	5.83	<5.87	6.37	0.13
7	0.038	–	6.50	6.43	7.18	0.12
8	0.043	–	5.83	5.83	6.35	0.13
9	0.060	–	5.38	<5.80	5.46	0.13
10	0.026	–	7.75	<8.16	8.74	0.10
11	0.021	0.051	4.38	4.37	5.36	0.18
12	0.040	0.074	3.33	<4.30	4.89	0.22
13	0.029	0.065	6.10	<6.47	7.07	0.12
14	0.009	0.082	7.78	<8.33	8.24	0.09
15	0.027	0.071	6.60	<7.38	8.03	0.11
16	0.033	0.081	6.25	<7.32	7.68	0.12

each simulation. Surface heat flow (q^{**}) and subsidence (ω^{**}) variations with respect to age (t^{**}) are derived from these structures. The subsidence is computed from the surface to the depth of the isotherm $T^{**} = T_q^{**}$, where T_q^{**} is defined in Section 2.5. Only two variables, T_i^* and z_{eq}^*, are necessary to adjust the heat flow $q^{**}(t^{**})$ given by the conductive model to $q^*(t^*)$ extracted from convective simulation (see Table 2). The equilibrium lithospheric thickness z_{eq}^* is found by inversion, while T_i^* is directly set to the measured temperature in the core flow. The discrepancy between models and simulations is measured on $1/q^*$ rather than q^* to minimize the differences near the ridge, where surface heat flow tends to infinity. Normalizations of $q^{**}(t^{**})$, $T^{**}(t^{**})$, and $\omega^{**}(t^{**})$ are then performed using the best fitting value of z_{eq}^* for each conductive model (see Table 2).

The surface heat flow adjustments between conductive models and simulations 16 (with bottom heating) and 7 (with internal heating) are shown in Fig. 12. In Fig. 13, the subsidence curves $\omega^*(t^*)$ obtained for each conductive models are compared to the result of the same simulations. The best model explaining the lithospheric cooling timescale of simulation 16 is the modified Chablis model. Note that the Plate model cooling timescale is too small to fit the cooling of a lithosphere overlying a convective mantle. Figs. 14–16 present the RMS differences on $1/q^{**}(t^{**})$, $\omega^{**}(t^{**})$, and $T^{**}(t^{**})$, respectively, between convective simulations and each conductive model. These figures clearly demonstrate that the best model to explain the lithospheric cooling in our convective simulations is the modified Chablis model. An imposed heat flow applied inside the lower part of the lithosphere is therefore a necessary boundary condition to model the conductive cooling of a lithosphere over a convecting mantle. For increasing equilibrium lithospheric thicknesses z_{eq}^*, the misfit between the Plate or Chablis models and the simulations increases (see Figs. 14–16). Indeed, the viscosity contrast in the asthenosphere below the ridge and below the lithosphere at equilibrium increases with z_{eq}^*. Therefore, the decrease of bottom heat flow with depth must be taken into account in conductive models. The equilibrium lithosphere thicknesses obtained for the best fitting models are listed in Table 5.

Table 5 also allows a comparison between the equilibrium surface heat flow obtained by the adjustment of the modified Chablis model to convective simulations, $q_{eq-conv}^*$. The q_{eq}^* is calculated using either $z_{eq}^* = T_i^*/q_{eq}^*$ for bottom heated cases and $z_{eq}^* = \left(q_{eq}^* - \sqrt{(q_{eq}^*)^2 - 2H^*T_i^*}\right)/H^*$ for internally heated cases. When the lithosphere did not reach thermal equilibrium before subduction, we give in Table 5 the surface heat flow near the convergent plate boundary as an upper bound for $q_{eq-conv}^*$. Note that q_{eq}^* and $q_{eq-conv}^*$ are in good agreement. The equilibrium

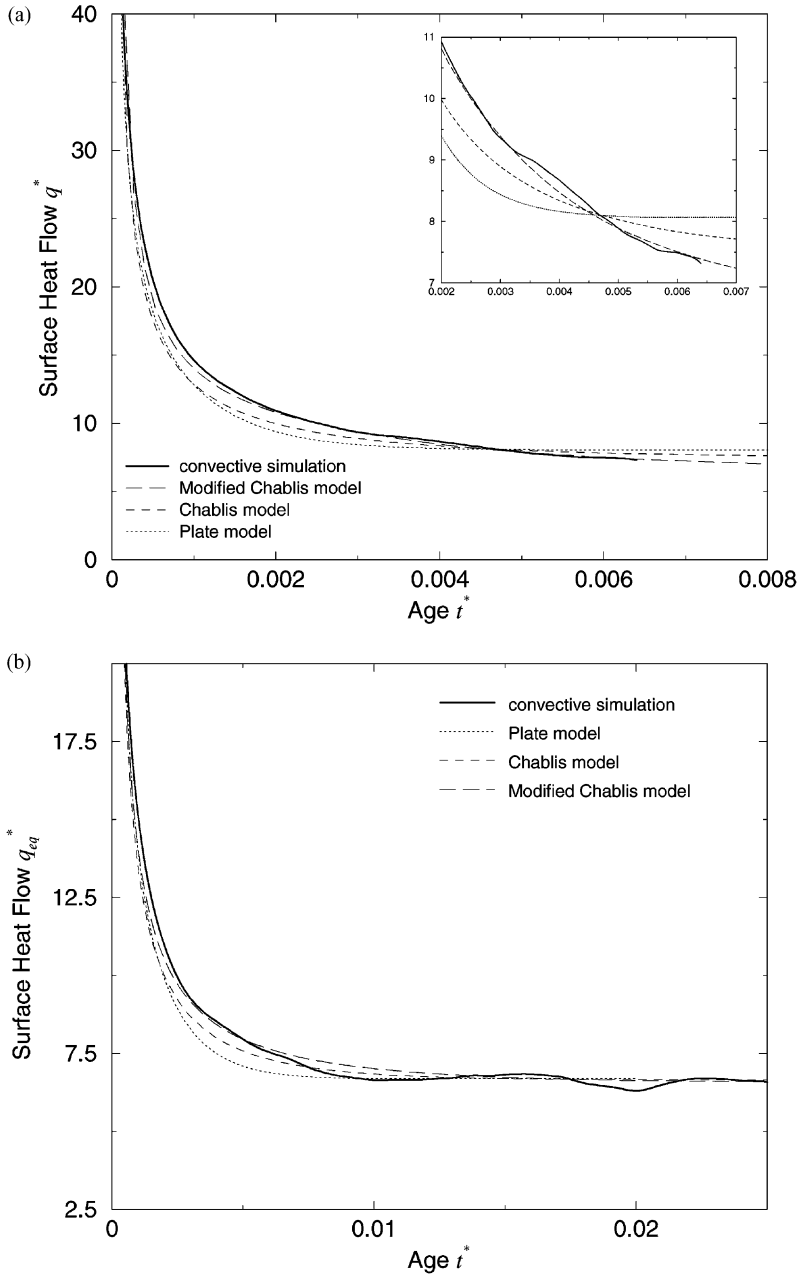

Fig. 12. Surface heat flow comparison between (a) simulation 16 (solid line) and the best fitting Plate (dotted line), Chablis (dashed line), and modified Chablis models (long dashed line), and (b) simulation 7 (solid line) and the conductive best fitting models. The upper right corner inset is a zoom.

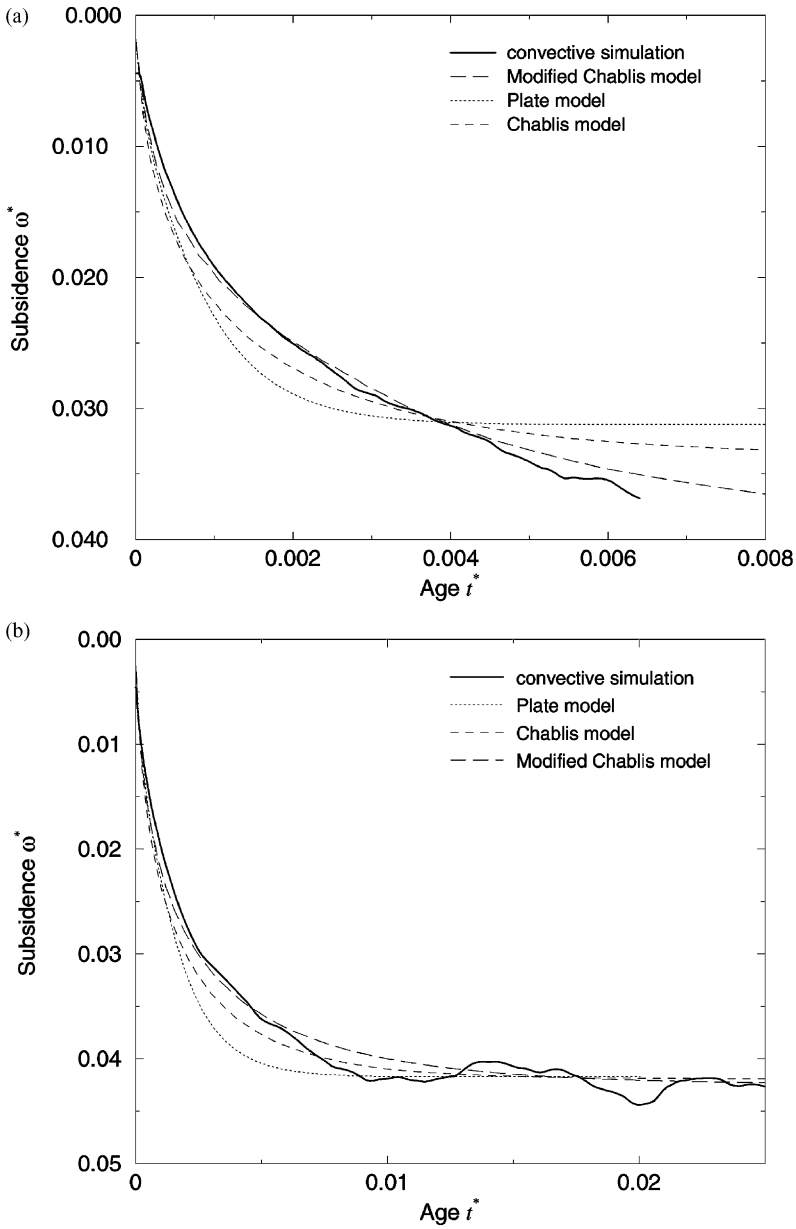

Fig. 13. Subsidence $\omega^*(t^*)$ comparison between (a) simulation 16 (solid line) and the best fitting Plate (dotted line), Chablis (dashed line), and modified Chablis models (long dashed line), and (b) simulation 7 (solid line) and the conductive best fitting models.

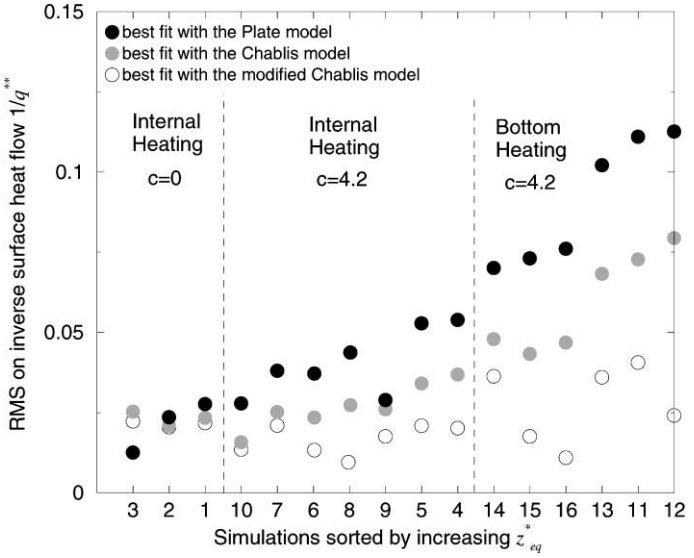

Fig. 14. RMS on the inverse surface heat flow between convective simulations and the best fitting Plate model (solid black circles), Chablis model (solid gray circles), or modified Chablis model (open circles). RMS are calculated as: RMS $= \sqrt{(\sum (X_{\text{conv}} - X_{\text{cond}})^2 / N)}$, where X is $1/q^{**}$ and N is the number of points. Simulations, referred by their number on the x-axis, are sorted by heating mode and values of c and, inside these categories, by increasing equilibrium lithospheric thickness z^*_{eq}.

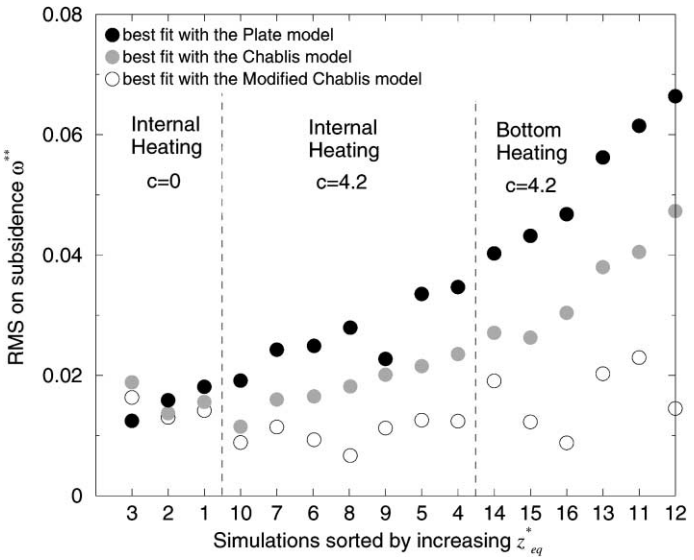

Fig. 15. RMS on subsidence between convective simulations and the best fitting conductive models. Simulations are referred by their number in Table 3. For the symbols and the x-axis legend, see Fig. 14, with $X = \omega^{**}$.

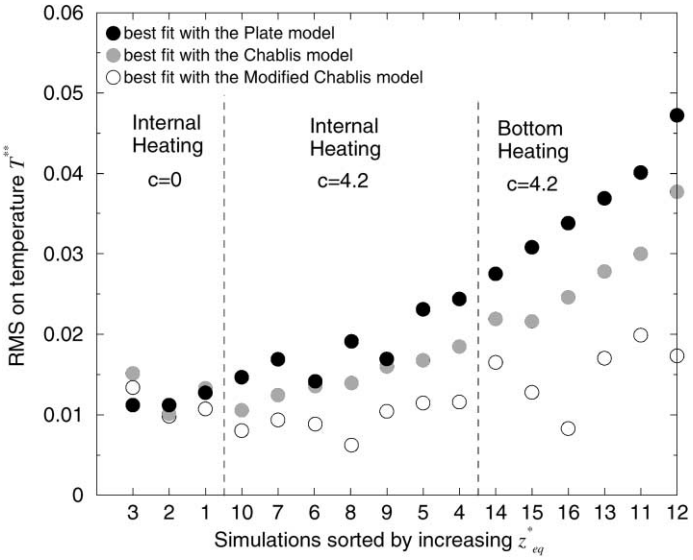

Fig. 16. RMS on temperature between convective simulations and the best fitting conductive models. Simulations are referred by their number in Table 3. For the symbols and the x-axis legend, see Fig. 14, with $X = T^{**}$.

surface heat flow can also be estimated from the relationships obtained using 2-D convection simulations without moving plates

$$q^*_{\mathrm{eq-calc}} = 0.52(Ra_0 \exp(bT^*_{\mathrm{i}} - cz^*_{\mathrm{eq}}))^{1/3} \times \left(b - \frac{c}{q^*_{\mathrm{eq-calc}}}\right)^{-4/3} \quad (6)$$

for a bottom heated fluid (see Dumoulin et al., 1999) and

$$q^*_{\mathrm{eq-calc}} = 0.51(Ra_0 \exp(bT^*_{\mathrm{i}} - cz^*_{\mathrm{eq}}))^{1/3} \times \left(b - \frac{c}{q^*_{\mathrm{eq-calc}}}\right)^{-4/3} + H^* z^*_{\mathrm{eq}} \quad (7)$$

for an internally heated fluid (Dumoulin, 2000). The values of $q^*_{\mathrm{eq-calc}}$, shown in Table 5, are often greater than q^*_{eq} and $q_{\mathrm{eq-conv}}$, especially for bottom heated simulations. We did not find any convincing evidence in our 2-D simulations that the difference $(q^*_{\mathrm{eq-calc}} - q^*_{\mathrm{eq}})$ is related to the shearing at the base of the lithosphere by large-scale convection.

5. Conclusion

Simulations of two-dimensional convection in a fluid heated from within or from below with a strongly temperature- and pressure-dependent viscosity have been performed, using a velocity imposed at the surface of the box. The purpose of these simulations was to study lithospheric cooling above a convective mantle. The two main findings of this study are as follows.

1. The base of the lithosphere is unstable at all ages (i.e. velocities cannot be neglected inside the base of the lithosphere), even if no dripping instabilities are seen close to the ridge. Near the ridge, the material flows along the slope defined by the lower part of the lithosphere with a velocity higher than the plate velocity and feeds the first instability.
2. A heat flow that decreases with depth and increases with asthenospheric temperature, applied inside the lower part of the lithosphere in conductive model, is necessary to explain the cooling time scales of the lithosphere in convective simulations.

Therefore, if the flattening of bathymetry, heat flow, and geoid in the oceanic lithosphere and the subsidence break in continental basins are due to

heat advection by a small-scale flow at the base of the lithosphere, then the modified Chablis model should be used to parameterize the lithospheric cooling through time.

Two main limitations apply to our study. At first, the modelled two-dimensional flow geometry might differ from that obtained in a three-dimensional box. Indeed, in 3-D convection experiments with an almost constant viscosity and with an imposed surface velocity, small-scale convection organizes after some time into rolls perpendicular to the ridge (Richter, 1973; Richter and Parsons, 1975), whereas in our study, small-scale convection is implicitly organized in rolls parallel to the ridge. The age of the first dripping instability could be different with rolls aligned along the shearing direction. However, 3-D numerical simulations of plume–lithosphere interaction with strongly temperature-dependent viscosity and with an upper moving plate, show that two different small-scale modes exist. As described above, the first mode consists of rolls aligned with the plate motion. For lower values of the viscosity below the lithosphere, small-scale convection is unsteady with a complex and time-dependent combination of downwelling sheets and drips (Moore et al., 1998). Furthermore, parameterization of the Nusselt versus Rayleigh number in the stagnant lid regime is identical in 3-D and 2-D at high Rayleigh numbers (Davaille and Jaupart, 1993; Dumoulin et al., 1999) and at low Rayleigh numbers (Reese et al., 1999; Dumoulin et al., 1999). The evolution of heat transfer by small-scale convection at the base of the cooling lithosphere should then be similar in 2-D and in 3-D convection simulations, although in some simulations the absolute values of heat transfer may be underestimated due to the shearing.

The second main limitation is that we did not introduce in our simulations density or viscosity variations induced by partial melting at the ridge. As the depleted mantle created by the partial melting at the ridge might be more viscous and, in the garnet stability field, less dense (Jordan, 1979) than the primitive mantle, it might inhibit the development of instabilities. As the heat flow brought by small-scale convection at the base of the lithosphere is shown to vary with the local viscosity, it should be smaller under the ridge. Therefore, the lithospheric cooling might then resemble that predicted by the Plate model. The effect on the convective heat transfer of such a viscosity increase at shallow depth linked with chemical variations is beyond the scope of the present paper but should be quantified in a future study.

Acknowledgements

The authors thank A. Davailte and an anonymous reviewer for their useful comments. We also thank K. Guibert for her contribution. The research was supported by a CNRS-INSU Interieur de la Terre grant.

References

Bird, P., 1998. Testing hypotheses on plate-driving mechanisms with global lithosphere models including topography, thermal structure, and faults. J. Geophys. Res. 103, 10115–10129.

Buck, W.R., 1985. When does small scale convection begin beneath oceanic lithosphere? Nature 313, 775–777.

Buck, W.R., Parmentier, E.M., 1986. Convection beneath young oceanic lithosphere: implications for thermal structure and gravity. J. Geophys. Res. 91, 1961–1974.

Cazenave, A., Lago, B., 1991. Long wavelength topography, seafloor subsidence and flattening. Geophys. Res. Lett. 18, 1257–1260.

Christensen, U.R., 1983. Convection in a variable-viscosity fluid: Newtonian versus power-law rheology. Earth Planet. Sci. Lett. 64, 153–162.

Christensen, U.R., 1984. Convection with pressure- and temperature-dependent non-Newtonian rheology. Geophys. J. Roy. Astron. Soc. 77, 343–384.

Crough, S.T., 1978. Thermal origin of mid-plate hot-spot swells. Geophys. J. Roy. Astron. Soc. 55, 451–470.

Davaille, A., Jaupart, C., 1993. Transient high-Rayleigh-number thermal convection with large viscosity variations. J. Fluid Mech. 253, 141–166.

Davaille, A., Jaupart, C., 1994. Onset of thermal convection in fluids with temperature-dependent viscosity: application to the oceanic mantle. J. Geophys. Res. 99, 19853–19866.

Davis, E.E., Lister, C.R.B., 1974. Fundamentals of ridge crest topography. Earth Planet. Sci. Lett. 21, 405–413.

Doin, M.P., Fleitout, L., 1996. Thermal evolution of the oceanic lithosphere: an alternative view. Earth Planet. Sci. Lett. 142, 121–136.

Doin, M.P., Fleitout, L., 2000. Flattening of the oceanic topography and geoid: thermal versus dynamic origin. Geophys. J. Int. 143, 582–594.

Doin, M.P., Fleitout, L., Christensen, U., 1997. Mantle convection and stability of depleted and undepleted continental lithosphere. J. Geophys. Res. 102, 2771–2787.

Dumoulin, C., 2000. Convection mantellique et structure de la lithosphère. Thèse de doctorat, Université Paris XI.

Dumoulin, C., Doin, M.P., Fleitout, L., 1999. Heat transport in stagnant lid convection with temperature- and pressure-dependent Newtonian or non-Newtonian rheology. J. Geophys. Res. 104, 12759–12778.

Eberle, M.A., Forsyth, D.W., 1995. Regional viscosity variations, small-scale convection and slope of the depth-age$^{1/2}$ curve. Geophys. Res. Lett. 22, 473–476.

Fleitout, L., Yuen, D., 1984. Secondary convection and the growth of oceanic lithosphere. Phys. Earth Planet. Inter. 36, 181–212.

Forsyth, D.W., 1977. The evolution of the upper mantle beneath mid-ocean ridges. Tectonophysics 38, 89–118.

Grasset, O., Parmentier, E.M., 1998. Thermal convection in a volumetrically heated, infinite Prandtl number fluid with strongly temperature-dependent viscosity. Implications for planetary thermal evolution. J. Geophys. Res. 103, 18171–18181.

Haxby, W.F., Weissel, J.K., 1986. Evidence for small-scale convection from seasat altimeter data. J. Geophys. Res. 91, 3507–3520.

Howard, L.N., 1964. Convection at high Rayleigh number. In: Gortler, H. (Ed.), Proceedings of the 11th International Congress on Applied Mechanics, Springer, New York.

Jaupart, C., Parsons, B., 1985. Convective instabilities in a variable viscosity fluid cooled from above. Phys. Earth Planet. Inter. 39, 14–32.

Jordan, T.H., 1979. Mineralogies, densities and seismic velocities of garnet lherzolites and their geophysical implications. In: Boyd, H.O.A., Meyer, F.R. (Eds.), The Mantle Sample: Inclusions in Kimberlites and Other Volcanics. Am. Geophys. Union, Washington, DC.

Kameyama, M., Ogawa, M., 2000. Transitions in thermal convection with strongly temperature-dependent viscosity in a wide box. Earth Planet. Sci. Lett. 180, 355–367.

King, S.D., Hager, B.H., 1990. The relationship between plate velocity and trench viscosity in Newtonian and power-law subduction calculations. Geophys. Res. Lett. 17, 2409–2412.

Lux, R., Davies, G., Thomas, J., 1979. Moving lithospheric plates and mantle convection. Geophys. J. Roy. Astron. Soc. 58, 209–228.

Moore, W.B., Schubert, G., Tackley, P., 1998. Three-dimensional simulations of plume–lithosphere interaction at the Hawaiian swell. Science 279, 1008–1011.

Morgan, J.P., Smith, W.H.S., 1992. Flattening of the sea-floor depth-age curve as a response to asthenospheric flow. Nature 359, 524–527.

Morris, S., Canright, D., 1984. A boundary-layer analysis of Bénard convection in a fluid of strongly temperature-dependent viscosity. Phys. Earth Planet. Inter. 36, 355–373.

Nataf, H.C., 1986. Eléments d'anatomie et de physiologie du manteau terrestre — tomographie sismique et convection expérimentale. Thèse d'état, Université Paris VI.

Nataf, H.C., Froidevaux, C., Levrat, J., Rabinowicz, M., 1981. Laboratory convection experiments: effect of lateral cooling and generation of instabilities in the horizontal boundary layers. J. Geophys. Res. 86, 6143–6154.

Parsons, B., McKenzie, D., 1978. Mantle convection and the thermal structure of the plates. J. Geophys. Res. 83, 4485–4496.

Reese, C., Solomatov, V., Baumgardner, J., Yang, W., 1999. Stagnant lid convection in a spherical shell. Phys. Earth Planet. Inter. 116, 1–7.

Richter, F.M., 1973. Convection and the large-scale circulation of the mantle. J. Geophys. Res. 78, 8735–8745.

Richter, F.M., Parsons, B., 1975. On the interaction of two scales of mantle convection. J. Geophys. Res. 80, 2529–2541.

Solomatov, V.S., 1995. Scaling of temperature- and stress-dependent viscosity convection. Phys. Fluids 7, 266–274.

Solomatov, V.S., Moresi, L.N., 2000. Scaling of time-dependent stagnant lid convection: application to small-scale convection on earth and other terrestrial planets. J. Geophys. Res. 105, 21795–21817.

Stein, C.A., Stein, S., 1992. A model for the global variation in oceanic depth and heat flow with lithospheric age. Nature 359, 123–129 .

Tackley, P.J., 2000. Mantle convection and plate tectonics: toward an integrated physical and chemical theory. Science 288, 2002–2007.

Turcotte, D.L., Oxburgh, E.R., 1967. Finite amplitude convective cells and continental drifts. J. Fluid Mech. 28, 29–42.

Wood, B.J., Yuen, D.A., 1983. The role of lithospheric phase transitions on seafloor flattening at old ages. J. Fluid Mech. 66, 303–314.

Yuen, D.A., Fleitout, L., 1984. Stability of the oceanic lithosphere with variable viscosity: an initial-value approach. Phys. Earth Planet. Inter. 343, 173–185.

Zhong, S., Gurnis, M., Moresi, L., 1998. Role of faults, nonlinear rheology, and viscosity structure in generating plates from instantaneous mantle flow models. J. Geophys. Res. 103, 15255–15268.